PAPER

One-step solvothermal synthesis of nickel–cobalt sulfides in a low coordination 1,4-dioxane solvent for supercapacitors

Yao Lei,[a] Qiwei Xu,[a] Yiru Miao*[a] and Jiarong Shi [ID] *[b]

Renowned for their exceptional specific capacity, high rate performance and good cycling stability, nickel–cobalt sulfides (NCSs) are highly promising electrode materials for supercapacitors. Unlike previous hydrothermal or solvothermal techniques that rely on solvents with strong polarity, high coordination ability and good solubility for synthesizing NCSs, this study employs solvents with low coordination and solubility ability for metal ions. These differences subsequently influence the macroscopic characteristics of the resultant materials. Specifically, the common solvent 1,4-dioxane with low coordination ability was employed. NCSs were synthesized using a straightforward one-step solvothermal method at different temperatures. NCS-180, synthesized at 180 °C, displays a sea urchin-like crystalline structure with aggregated linear nickel cobalt sulfide and demonstrates superior electrochemical performance. At a current density of 1 A g^{-1}, it exhibits a specific capacity of 664.30 C g^{-1}. Moreover, after enduring 5000 cycles at 10 A g^{-1}, its capacity retention rate remains at 97.99%. Additionally, a dual-electrode configuration was constructed, utilizing NCS-180 as the cathode and activated carbon (AC) as the anode. The findings reveal that the NCS-180//AC system demonstrates a notable energy density of 50.35 Wh kg^{-1} at a power density of 750 W kg^{-1}. Furthermore, after enduring 6000 cycles at 10 A g^{-1}, the system retains a capacitance retention rate of 93.30%.

Introduction

In recent years, metal sulfides have emerged as a novel class of nanomaterials with widespread applications in energy storage. Their significant advantages (including high power density, prolonged cycle life, and environmental benignity) have enabled their extensive utilization in electrode materials for supercapacitors. Among the various metal sulfides, bimetallic sulfides exhibit superior performance compared to their mono-metallic counterparts.[1] Studies have demonstrated that multi-component compounds can effectively narrow the optical band gap width of materials, thereby enhancing their conductivity. Moreover, synergistic interactions among the different components further amplify the electrochemical activity of these compounds.[2,3] For instance, nickel–cobalt sulfides (NCSs), notable bimetallic sulfides, exhibit high specific capacity, exceptional rate performance and robust cycling stability, rendering them promising candidates for supercapacitor electrode materials.[4] Therefore, the development of synthetic methods

for bimetallic sulfides has emerged as a focal point of research in this field.

In prior research endeavors, NCSs exhibiting diverse morphologies have been synthesized utilizing either hydrothermal or solvothermal techniques.[5] And these studies suggest that differences in the physico-chemical properties of solvents, including polarity, coordination ability and solubility for metal ions, can significantly impact crystal growth,[6,7] leading to notable variations in the morphologies and electrochemical properties of NCSs. In 2013, Jiang and colleagues pioneered the preparation of sea urchin-like nickel–cobalt sulfide *via* a two-step hydrothermal process, which is first conducting hydrothermal synthesis of cobalt–nickel hydroxide, followed by sulfidation.[8] Employing a method similar to the aforementioned synthesis process, Dong and colleagues successfully synthesized NiCo$_2$S$_4$ with various morphologies (tube-like, flower-like, sea urchin-like and cubic-like) by adjusting the ratio of deionized water to ethanol or ethylene glycol.[9] Different from the above methods, Mu's group synthesized sea urchin-like NiCo$_2$S$_4$ *via* a one-step solvothermal process using polyethylene glycol.[10] The polyethylene glycol is an efficient shape-control agent for nanoparticle formation because of its two –OH groups, which can be selectively adsorbed on certain faces of a crystal to increase the growth rate of these faces.

[a] State Key Laboratory of Power Transmission Equipment Technology, School of Electrical Engineering, Chongqing University, Chongqing, 400044, China

[b] School of Chemistry and Chemical Engineering, Chongqing University, Chongqing, 401331, China. E-mail: 1138416789@qq.com

Additionally, Huang's group synthesized the flaky attached hollow-sphere structure $NiCo_2S_4$ using a mixed solvent of isopropanol and triethylene glycol.[11] Recently, Mohamed's group synthesized nickel–cobalt sulfide nanoparticles through a one-step solvothermal process, employing ethylene glycol as the solvent.[12] However, all the solvents employed in the past exhibited strong polarity, high coordination ability and good solubility for metal ions, such as deionized water, ethanol, ethylene glycol, polyethylene glycol, isopropanol and triethylene glycol.[13–16] In contrast, there has been a significant lack of research studies on the utilization of solvents with low coordination ability and poor solubility for metal ions. Within these solvents, due to the weak coordination effect of the solvent, metal ions exhibit a limited tendency towards solvation, leading to a decreased solubility of the metal ions. As a result, during the solvothermal synthesis of nickel–cobalt sulfides (NCSs), NCSs are present in the solvent at a low level of supersaturation. It has been proven that at this low supersaturation, anisotropic low-dimensional growth may be preferable.[6,7,9] Consequently, the effort to use these solvents in the synthesis of NCSs will provide additional synthetic routes for fabricating NCSs with specific structures and properties.

Based on the above idea, we utilized 1,4-dioxane with weak coordination ability as the solvent, with thiourea serving as the sulfur precursor, to synthesize NCSs *via* a one-step solvothermal process (Fig. 1). Fortunately, linear nickel cobalt sulfide was successfully synthesized and subsequently aggregated to form a sea urchin-like morphology. The nickel–cobalt sulfide synthesized at 180 °C (NCS-180) exhibits a higher degree of crystallinity, subsequently demonstrating superior electrochemical performance. In detail, NCS-180 possesses a specific capacity of 664.30 C g^{-1} at a current density of 1 A g^{-1}. It retains a capacity retention rate of 97.99% after 5000 cycles at a current density of 10 A g^{-1}. Furthermore, the dual-electrode system, which comprises NCS-180 as the cathode and activated carbon as the anode, demonstrates a remarkable energy density of 50.35 Wh kg^{-1} when operated at a power density of 750 W kg^{-1}. Notably, this system retains a capacity retention rate of 93.30% even after undergoing 6000 cycles at a current density of 10 A g^{-1}, highlighting its long-term performance stability.

Experimental

0.5 mmol of $NiCl_2 \cdot 6H_2O$, 1 mmol of $CoCl_2 \cdot 6H_2O$, and 2 mmol of thiourea were added to 25 mL of 1,4-dioxane. After stirring at room temperature for 30 minutes, the mixture was transferred to a 100 mL Teflon-lined stainless steel autoclave and reacted at 140 °C, 160 °C and 180 °C for 12 hours, respectively. Upon completion of the reactions, the products were collected, washed with ethanol and water, and dried in an oven at 60 °C for 12 hours. The obtained products were denoted as NCS-140, NCS-160 and NCS-180, respectively. To highlight the performance of nickel–cobalt sulfides, nickel sulfide (designated as NS) and cobalt sulfide (designated as CS) were synthesized using the same solvent under conditions of 180 °C.
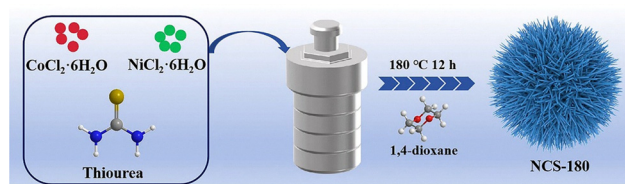

Fig. 1 Schematic of the formation process of NCS-180.

Results and discussion

The surface morphology of the materials was investigated using field emission scanning electron microscopy (FESEM). Fig. 2a and b exhibit the SEM images of NCS-140, which clearly demonstrate that the product synthesized at 140 °C comprises two distinct morphologies: needle-like structures and bulk structures. In contrast, NCS-160 and NCS-180 exhibit a consistent morphology, both displaying urchin-like structures formed by the aggregation of nanoneedles. This unique structure serves to enhance the material's specific surface area, increase the number of active reaction sites, and improve its specific capacity. As illustrated in Fig. S1–S3, NCS-140, NCS-160 and NCS-180 all contain the elements Ni, Co, and S.

To further elucidate the morphological and microstructural characteristics of the synthesized cobalt–nickel sulfide materials, transmission electron microscopy (TEM) analyses were performed on NCS-180 and NCS-160, as illustrated in Fig. 3 and Fig. S6, respectively. Fig. 3a shows the electron diffraction pattern of NCS-180, clearly revealing multiple diffraction rings that correspond to the (111), (220), (311), (400), (511) and (440)
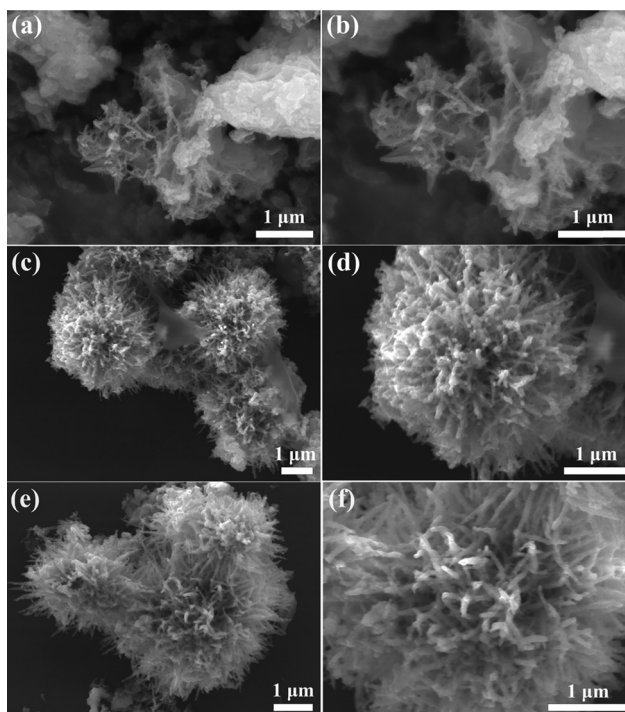

Fig. 2 (a) and (b) SEM images of NCS-140; (c) and (d) SEM images of NCS-160; and (e) and (f) SEM images of NCS-180.
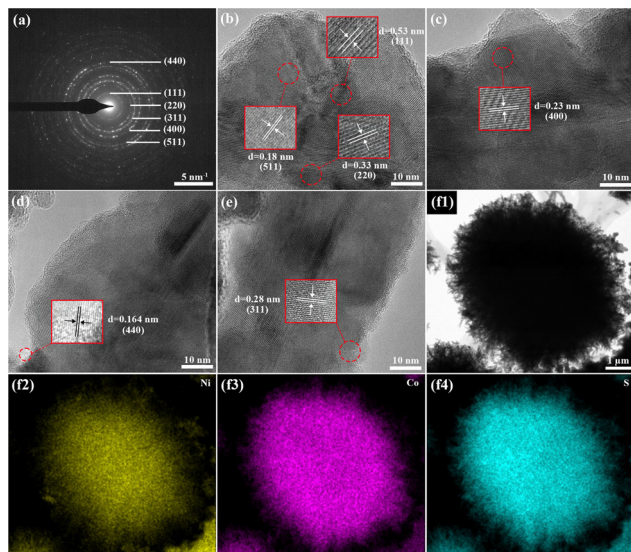
Fig. 3 Electron diffraction pattern (a); HRTEM images (b)−(e); TEM image (f1); EDS elemental mapping images (f2)−(f4) of NCS-180.

Fig. 4 (a) XRD patterns of NCS-140, NCS-160, NCS-180; (b)−(d) XPS spectra of NCS-180.

crystal planes of $NiCo_2S_4$ (JCPDS No. 20-0782). The high-resolution image of NCS-180 further exhibits distinct lattice fringes with measured interplanar spacings of 0.53, 0.33, 0.28, 0.23, 0.18 and 0.164 nm, aligning with the crystal planes of $NiCo_2S_4$.[17] Fig. 3f1 illustrates that NCS-180 possesses a sea urchin-like morphology, which is consistent with the observations from scanning electron microscopy. Fig. 3f2–f4 present the elemental mappings of Ni, Co and S, respectively, demonstrating a clear and homogeneous distribution of these elements. Fig. S6 displays the transmission electron microscopy results of NCS-160. In comparison to NCS-180, the electron diffraction pattern exhibits fewer and darker diffraction rings, corresponding solely to the (400) and (440) crystal planes of $NiCo_2S_4$. Furthermore, the high-resolution image of NCS-160 reveals the presence of partially amorphous regions, indicating a relatively lower crystallinity compared to NCS-180. This indicates that in 1,4-dioxane, although cobalt–nickel sulfide can already be synthesized at a lower temperature (160 °C), its crystallinity is relatively poor. By further increasing the reaction temperature to 180 °C, cobalt–nickel sulfide with higher crystallinity can be obtained.

Subsequently, further verification of the samples' structural features was conducted using X-ray powder diffraction (XRD). Fig. 4a presents the XRD patterns of NCS-140, NCS-160 and NCS-180, revealing distinct diffraction peaks for products synthesized at varying temperatures. Specifically, the diffraction peaks of NCS-180 at angles of 16.35°, 26.86°, 31.53°, 38.23°, 50.33° and 55.11° align with the (111), (220), (311), (400), (511) and (440) crystal planes of $NiCo_2S_4$ (JCPDS No. 20-0782),[18,19] respectively, and the absence of additional peaks indicates a homogeneous material composition. In comparison to NCS-180, NCS-160 exhibits an absence of the diffraction peak corresponding to the (111) crystal plane. While the positions of the remaining peaks remain largely unchanged, the diffraction peak intensity of NCS-160 is notably weaker than that of NCS-180, suggesting a superior crystallinity for NCS-180. This observation aligns with the findings
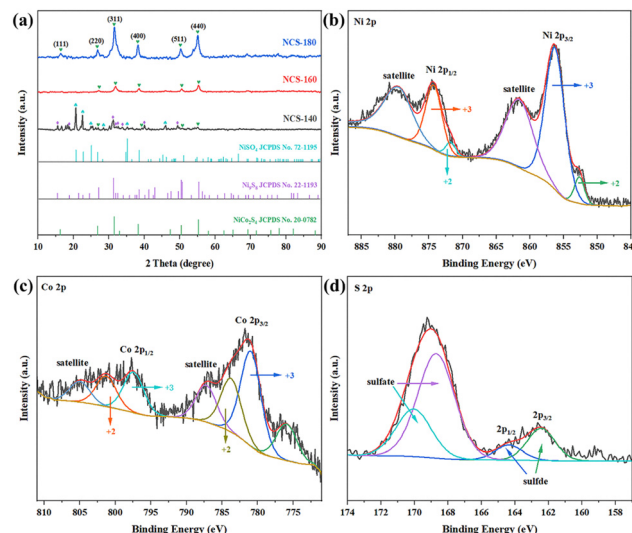
derived from transmission microscopy. The XRD pattern of NCS-140 enables the identification of characteristic peaks associated with three substances. Notably, the relatively weak characteristic peaks of $NiCo_2S_4$ might be explained by its lower abundance in the NCS-140 sample. The diffraction peaks at 20.60°, 22.55°, 24.94°, 28.45°, 35.12° and 46.00° correspond to the (110), (020), (111), (002), (112) and (040) crystal planes of $NiSO_4$ (JCPDS No. 72-1195),[20] whereas those at 15.51°, 18.84°, 31.29°, 32.04°, 32.54°, 33.99°, 40.09° and 49.51° match the (111), (002), (222), (132), (023), (203), (114) and (115) crystal planes of Ni_9S_8 (JCPDS No. 22-1193).[21,22] These findings indicate that NCS-140 is a mixture, suggesting that a reaction temperature that is too low is detrimental to the formation of $NiCo_2S_4$.

To investigate the elemental composition and chemical valence states of NCS-180, X-ray photoelectron spectroscopy (XPS) analysis was conducted. The outcomes of this analysis are depicted in Fig. 4b–d. The results confirm the presence of nickel, cobalt and sulfur in NCS-180, which is consistent with the previous EDS analysis. Fig. 4b illustrates the Ni 2p orbital spectrum, revealing two distinct spin–orbit doublet peaks for NCS-180. The peaks observed at 852.63 eV and 871.78 eV are ascribed to Ni^{2+}, whereas those at 856.27 eV and 874.27 eV are attributed to Ni^{3+}. This finding suggests the coexistence of both Ni^{2+} and Ni^{3+} within NCS-180. Additionally, the peaks at 861.56 eV and 879.53 eV are shake-up satellite peaks of the Ni 2p orbital.[23,24] Fig. 4c displays the Co 2p orbital spectrum. The peaks observed at 780.94 eV and 797.42 eV in NCS-180 are characteristic of Co^{3+}, while those at 783.73 eV and 801.29 eV correspond to the characteristic peaks of Co^{2+} within NCS-180.[25,26] Fig. 4d presents the S 2p orbital spectrum, where the peaks at binding energies of 162.44 eV and 164.36 eV in NCS-180 represent $2p_{3/2}$ and $2p_{1/2}$ of the metal sulfide, respectively.[27,28] These results further confirm that the synthesized material is cobalt–nickel sulfide. However, the spectral peaks situated at 168.70 eV and 170.04 eV are associated with
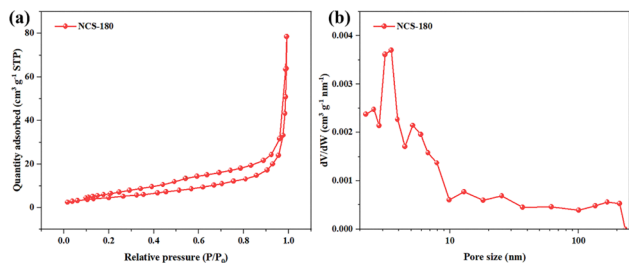
Fig. 5 (a) N$_2$ adsorption/desorption curve; (b) pore size distribution curve of NCS-180.

metal sulfate.[29,30] This observation can be attributed to the partial oxidation of sulfur, a commonly encountered phenomenon in the synthesis process of cobalt–nickel sulfide.[31–33] To further confirm the generation of sulfate ions, X-ray single crystal diffraction analysis was conducted on the precipitated single crystals obtained from the washed NCS-180 crude product solution. The results identified the crystal structure as cobalt sulfate hexahydrate (CoSO$_4$·6H$_2$O) (Fig. S11), indicating that sulfate radicals were indeed generated during the synthesis of NCS-180.

Additionally, the specific surface area and pore size distribution of NCS-180 were characterized through N$_2$ adsorption/desorption experiments, with the results illustrated in Fig. 5. The N$_2$ adsorption/desorption isotherm depicted in Fig. 5a displays a pronounced hysteresis loop, indicating the existence of mesoporous structures within NCS-180. The experimentally determined specific surface area of NCS-180 is 17.60 m^2 g^{-1}. An examination of the pore size distribution profile in Fig. 5b reveals

that NCS-180 exhibits a relatively broad pore size distribution, with the most probable BJH pore diameter calculated to be 3.49 nm. Collectively, these findings indicate that NCS-180 possesses a substantial surface area, which can accommodate numerous active reaction sites, and its mesoporous architecture facilitates the provision of transport pathways for electrolyte ions.

After confirming the morphology and microstructure of the synthesized material, we proceeded to investigate its electrochemical properties. These properties were evaluated using a three-electrode system. This setup included a 1 cm^2 platinum plate serving as the counter electrode, an Hg/HgO electrode functioning as the reference electrode, and 3 M KOH as the electrolyte solution. A series of electrochemical measurements were performed on the samples, including cyclic voltammetry (CV), galvanostatic charge–discharge (GCD) testing and electrochemical impedance spectroscopy (EIS).

Fig. 6a and b show the cyclic voltammetry (CV) curves of NCS-140, NCS-160, NCS-180, NS and CS, respectively, at a scan rate of 5 mV s^{-1}. The presence of a pair of redox peaks in all five materials clearly indicates their pseudocapacitive characteristics. Notably, as the reaction temperature increases, the area enclosed by the CV curves for these materials expands. Given that the specific capacitance of a material is directly proportional to the area of its CV curve, it is evident that NCS-180 exhibits the highest specific capacitance. Additionally, the CV curve area of NCS-180 surpasses that of NS and CS, indicating that bimetallic sulfides outperform monometallic sulfides in terms of performance. XPS analysis reveals that NCS-180 contains Ni^{2+}, Ni^{3+}, Co^{2+} and Co^{3+} ions, suggesting the occurrence
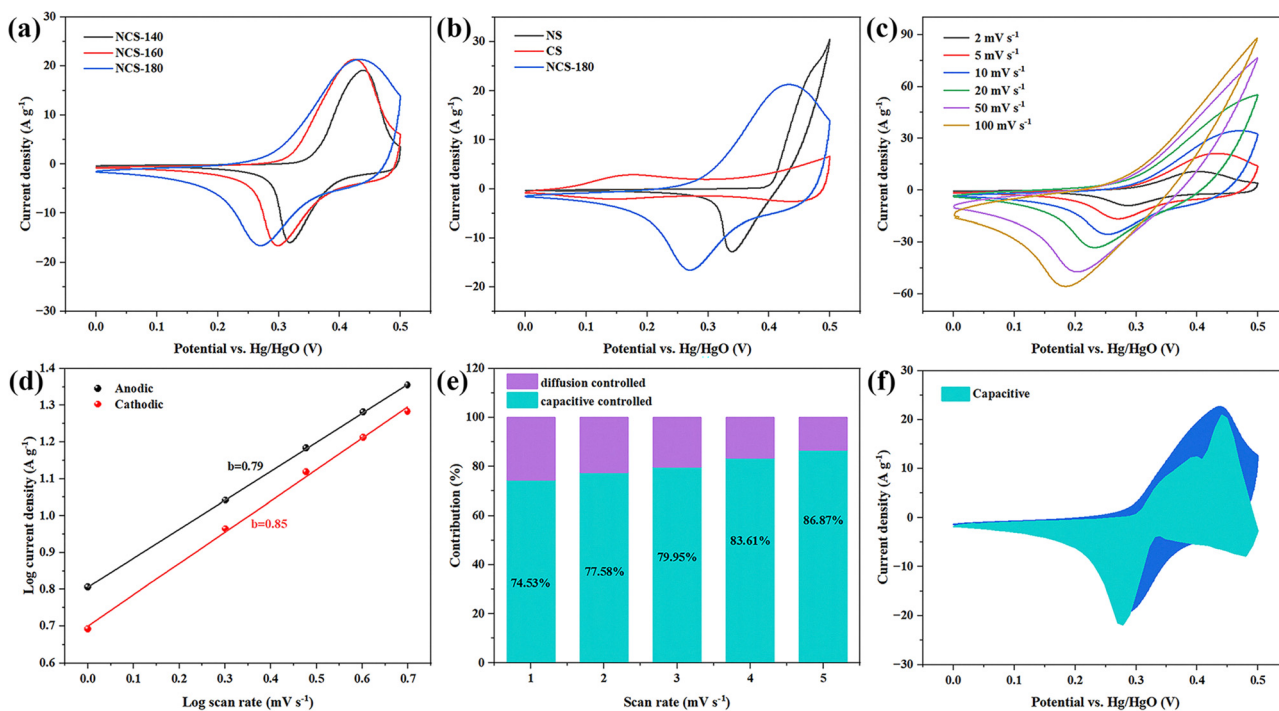

Fig. 6 (a) CV curves of NCS-140, NCS-160, NCS-180 at 5 mV s^{-1}; (b) CV curves of NS, CS, NCS-180 at 5 mV s^{-1}; (c) CV curves of NCS-180 at different scan rates; (d) dependence of log current on the log scan rate for NCS-180; (e) contribution ratio of capacitance and diffusion-controlled parts to the NCS-180 electrode at different scan rates; (f) capacitive contribution of NCS-180 at 5 mV s^{-1}.

of reversible conversions among Ni^{2+}/Ni^{3+}, Co^{2+}/Co^{3+} and Co^{3+}/Co^{4+} in NCS-180.[19] Fig. 5c illustrates the CV curves of NCS-180 at various scan rates. As the scan rate increases, the anodic oxidation peak shifts towards a higher potential, while the cathodic reduction peak shifts towards a lower potential. The integral area of the CV curves augments with the scan rate, and redox peaks remain observable even at high scan rates, demonstrating the material's exceptional rate capability.

As depicted in eqn (1), an in-depth investigation of the energy storage mechanism of NCS-180 was conducted by examining the linear relationship between the logarithm of current and the logarithm of scan rate.[34] The slope b in eqn (1) is indicative of electrode kinetics. Prior research study has established that a b-value of 0.5 signifies that the electrode material is predominantly controlled by diffusion, whereas a b-value of 1 implies full capacitance control. By analyzing the peak currents of the CV curves at scan rates spanning from 1 to 5 mV s^{-1}, the calculated b-values were determined to be 0.79 for the anodic peak and 0.85

for the cathodic peak (Fig. 6d), respectively. These b-values, situated between 0.5 and 1, indicate that the energy storage mechanism of NCS-180 encompasses both capacitance control and diffusion control. The proportions of capacitance control and diffusion control at scan rates ranging from 1 to 5 mV s^{-1} were computed using eqn (2) and (3), with the outcomes presented in Fig. 6e.[35] As the scan rate escalates, the capacitance contribution progressively increases. This phenomenon can be attributed to the diminished diffusion capacity of the material at elevated current densities. As shown in Fig. 6e and f, the notably higher proportion of capacitance contribution, in comparison to diffusion control, suggests that the primary capacity contribution of NCS-180 stems from surface capacitance.

$$\log i = b \log v + \log a \tag{1}$$

$$i = k_1 v + k_2 v^{0.5} \tag{2}$$

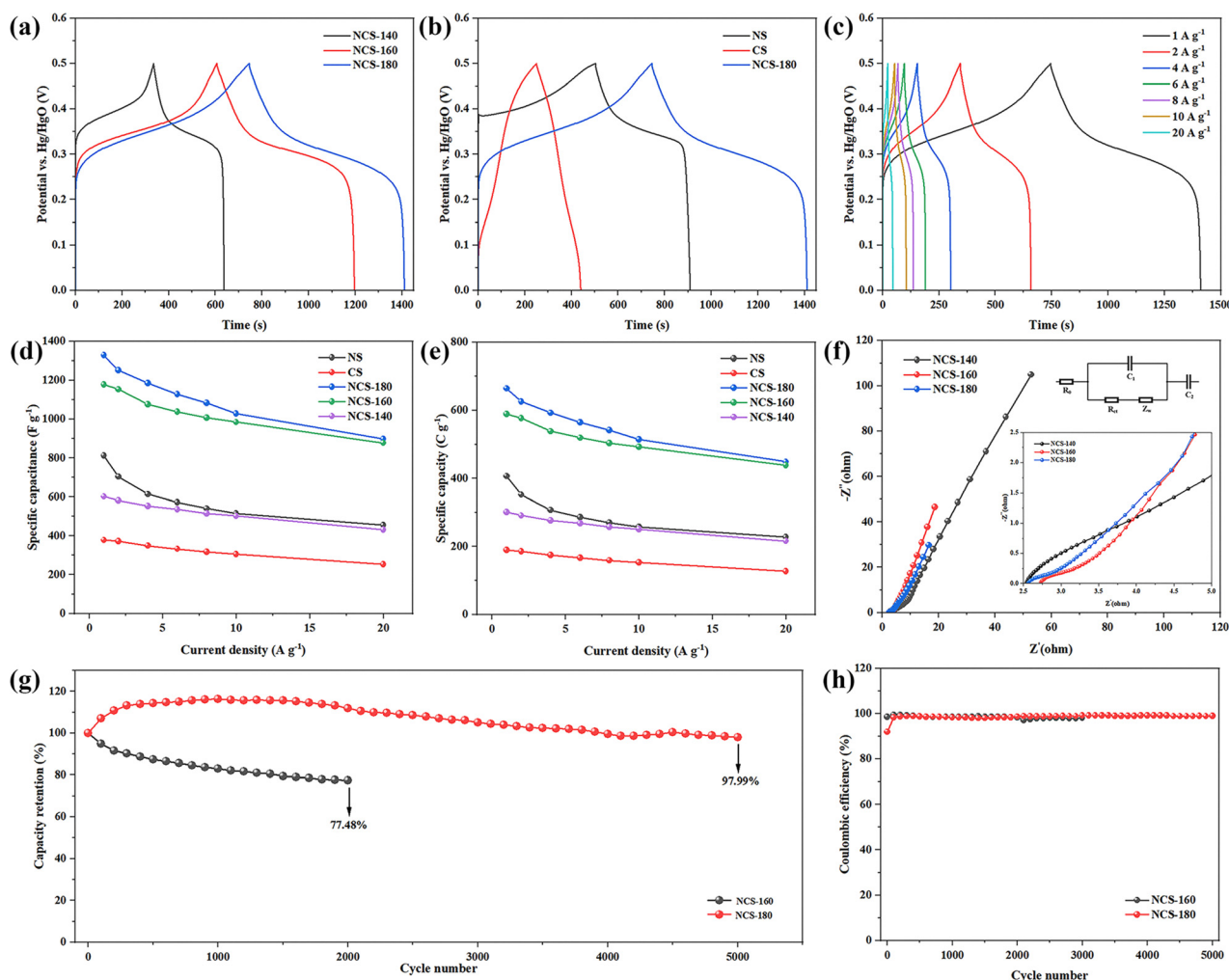$$\frac{i}{v^{0.5}} = k_1 v^{0.5} + k_2 \tag{3}$$

Fig. 7 (a) GCD curves of NCS-140, NCS-160, NCS-180 at 1 A g^{-1}; (b) GCD curves of NS, CS, NCS-180 at 1 A g^{-1}; (c) GCD curves of NCS-180 at different current density; (d) and (e) specific capacitance and capacity of NS, CS, NCS-180, NCS-160, NCS-140 at different current density; (f) EIS curves of NCS-140, NCS-160, NCS-180; (g) and (h) cycling life of NCS-160, NCS-180 at 10 A g^{-1}.

To further validate the electrochemical characteristics of the materials, galvanostatic charge–discharge tests were conducted. Fig. 7a presents the charge–discharge profiles of NCS-140, NCS-160 and NCS-180 at a current density of 1 A g^{-1}. All three materials demonstrate distinct charge–discharge platforms, indicative of redox reactions occurring during the charging and discharging processes. Consequently, these materials are classified as battery-type materials, which aligns with the findings obtained from cyclic voltammetry curves.[36,37] The specific capacities of NCS-140, NCS-160 and NCS-180, calculated at a current density of 1 A g^{-1}, are 301.07 C g^{-1} (602.14 F g^{-1}), 589.17 C g^{-1} (1178.34 F g^{-1}) and 664.30 C g^{-1} (1328.60 F g^{-1}), respectively. An increase in reaction temperature results in a gradual enhancement of the materials' specific capacities, suggesting that temperature plays a significant role in influencing electrochemical performance. Specifically, a sharp increase in specific capacity is observed when the reaction temperature rises from 140 °C to 160 °C. This may be attributed to the unfavorable conditions at 140 °C for the formation of NiCo$_2$S$_4$, as evidenced by the presence of numerous impurity peaks in the XRD data for NCS-140, indicating an inhomogeneous composition. In contrast, NCS-160 and NCS-180 exhibit only the characteristic peaks of NiCo$_2$S$_4$. When the reaction temperature further increases from 160 °C to 180 °C, the specific capacity increase is relatively modest. This could be due to the fact that uniform NiCo$_2$S$_4$ can already be formed at 160 °C, and any further increase in temperature primarily enhances the crystallinity of the material without altering its morphology and composition significantly, leading to comparable specific capacities. Fig. 7b depicts the galvanostatic charge–discharge curves for NS, CS, and NCS-180, with NCS-180 exhibiting the longest discharge time. Compared to single-metal sulfides, bimetallic sulfides possess a greater number of reactive sites, which translates to higher specific capacities.

The charge–discharge curves of NCS-180 at different current densities, as well as the specific capacitance and specific capacity of several materials at various rates, are shown in Fig. 7c–e. Specifically, the specific capacities of NCS-180 at current densities of 1, 2, 4, 6, 8, 10 and 20 A g^{-1} are 664.30 C g^{-1} (1328.60 F g^{-1}), 625.80 C g^{-1} (1251.60 F g^{-1}), 592.53 C g^{-1} (1185.06 F g^{-1}), 564.40 C g^{-1} (1128.80 F g^{-1}), 541.87 C g^{-1} (1083.74 F g^{-1}), 514.33 C g^{-1} (1028.66 F g^{-1}) and 448.67 C g^{-1} (897.34 F g^{-1}), respectively. When the current density increases to 10 A g^{-1}, the specific capacity of NCS-180 is nearly identical to that of NCS-160. At a high current density of 10 A g^{-1}, the capacity retention rates for NCS-160 and NCS-180 are 83.56% and 77.42%, respectively. The high crystallinity of NCS-180 leads to a decreased diffusion rate, whereas NCS-160 contains amorphous structures which lack long-range order, allowing ions to diffuse in multiple directions and thus exhibiting higher rate performance. In comparison to previously reported studies, the nickel–cobalt sulfides synthesized in this work demonstrate superior electrochemical performance, as summarized in Table 1.

Fig. 7f illustrates the Nyquist plots for NCS-140, NCS-160 and NCS-180. These plots were analyzed through equivalent circuit fitting using the commercial software ZSimpWin to assess the impedance performance of the materials. The ohmic

Table 1 A comparison of electrochemical storage performance of nickel cobalt sulfides

Materials	Current density (A g^{-1})	Electrolyte	Specific capacitance	Ref.
NiCo$_2$S$_4$	1	6 M KOH	1224 F g^{-1}	38
NCS	1	6 M KOH	899 F g^{-1}	39
NiCo$_2$S$_4$/rGO	1	6 M KOH	1072 F g^{-1}	40
NiCoS/CNFs	1	1 M KOH	763 F g^{-1}	41
NiCo$_2$S$_4$/Co$_2$C	1	6 M KOH	970 F g^{-1}	42
NiCo$_2$S$_4$ NCAs/3D Gr	1	6 M KOH	948.9 F g^{-1}	43
NiCo$_2$S$_4$@NiFe LDH	1	3 M KOH	827 F g^{-1}	44
NiCo$_2$S$_4$@NGO/CMC	2	3 M KOH	767 F g^{-1}	45
NiCo$_2$S$_4$	5	3 M KOH	554.54 F g^{-1}	46
NiCo$_2$S$_4$ NSs	1	2 M KOH	957 F g^{-1}	47
NCS-180	1	3 M KOH	664.30 C g^{-1} (1328.60 F g^{-1})	This work

internal resistance (R_0) of the three-electrode system, which encompasses the electron transport impedance within the electrode and solution resistance, is represented by the intercept of the capacitive reactance arc in the high-frequency region with the real axis. Specifically, the R_0 values for NCS-140, NCS-160 and NCS-180 were determined to be 2.67, 2.77 and 2.59 Ω, respectively. In the mid-to-high frequency region, the capacitive reactance arc can be modeled as a capacitor in parallel with a resistor, where the resistor signifies the charge transfer resistance (R_{ct}) of the material. The fitted R_{ct} values for NCS-140, NCS-160 and NCS-180 were found to be 1.34, 0.29 and 0.22 Ω, respectively, with NCS-180 demonstrating the lowest charge transfer resistance. High crystallinity promotes electron conduction and subsequently enhances the conductivity of the material. Consequently, NCS-180 demonstrates the lowest charge transfer resistance among the samples. The oblique line observed in the low-frequency region indicates the diffusion impedance of electrolyte ions within the electrode material. This diffusion impedance is correlated with the slope of the line, where a steeper slope corresponds to a smaller diffusion impedance.[48] As can be observed from the graph, the diffusion resistance of NCS-160 is smaller than that of NCS-180, which corroborates the conclusion that materials with lower crystallinity exhibit superior diffusion properties. This observation aligns well with the outcomes of the rate capability assessments.

To assess the stability of the materials, cyclic stability tests were conducted on both NCS-160 and NCS-180. Galvanostatic charge–discharge tests, employing a current density of 10 A g^{-1}, were executed on these materials, and the results are presented in Fig. 7g and h. The capacity retention rate of NCS-180 displayed a trend of initial increase followed by a decline, ultimately reaching 97.99% after 5000 cycles. This observation underscores the material's excellent cyclic stability. Conversely, the capacity retention rate of NCS-160 exhibited a consistent decline, culminating in a retention rate of 77.48% after 2000 cycles. The variation in stability observed between the two materials can be ascribed to their differing crystallinity. NCS-160, with its lower crystallinity and poor structural stability, undergoes irreversible phase transformations during cycling,
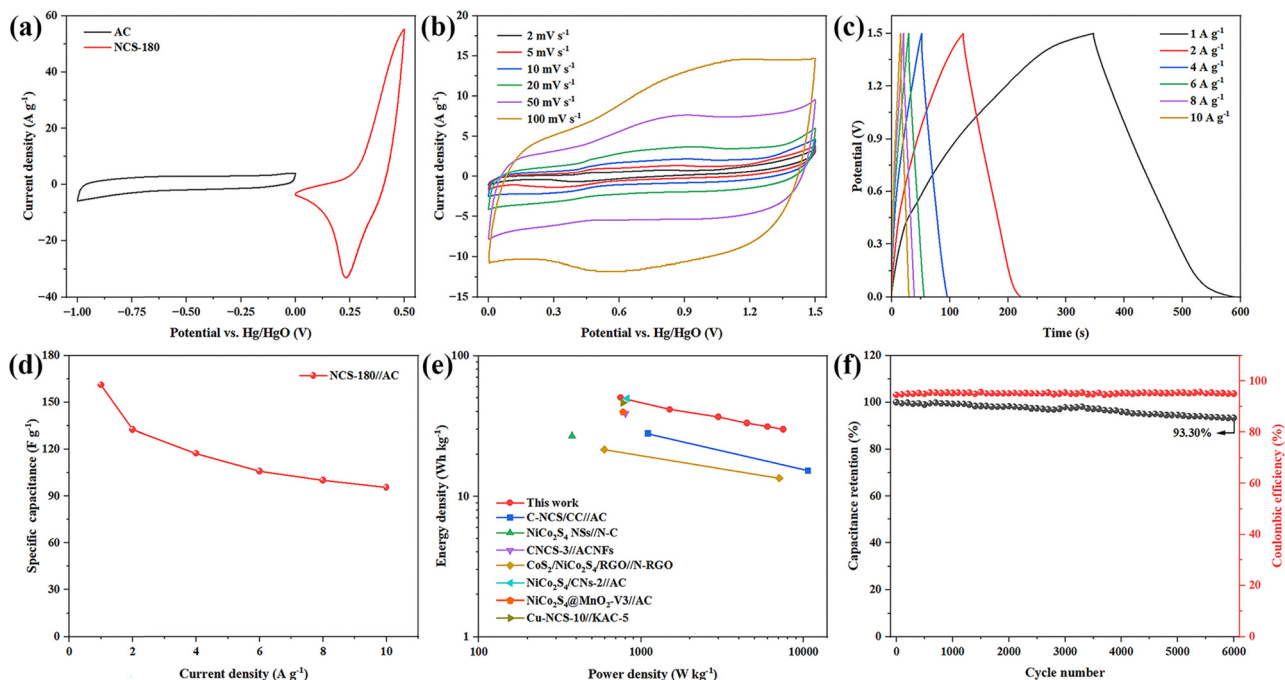
Fig. 8 (a) CV curves of AC, NCS-180 at 20 mV s^{-1}; (b) CV curves of NCS-180//AC at different scan rates; (c) GCD curves of NCS-180//AC at different current density; (d) specific capacitance of NCS-180//AC at different current density; (e) Ragone plot for recent asymmetric devices; (f) cycling life of NCS-180//AC at 10 A g^{-1}.

ultimately leading to capacity degradation.[49,50] Conversely, NCS-180 exhibits higher crystallinity and anisotropic crystalline structures, which impede ion diffusion, causing ions to diffuse slowly within NCS-180 and resulting in an initial increase in capacity during cycling. Furthermore, materials with elevated crystallinity possess a more robust lattice structure, rendering them resistant to structural collapse during cycling, and thus contributing to superior cycle stability.

Finally, to explore the energy storage properties of NCS-180, an asymmetric supercapacitor was constructed utilizing NCS-180 as the cathode, activated carbon as the anode, and a 3 M KOH solution as the electrolyte (Fig. 8). By considering the voltage windows of both activated carbon and NCS-180, the optimal voltage window for the NCS-180//AC asymmetric supercapacitor was established at 1.5 V (Fig. 8a). Analysis of the cyclic voltammetry (CV) curves of NCS-180//AC at varying scan rates revealed no notable polarization within the voltage range of 0 to 1.5 V (Fig. 8b). Fig. 8c depicts the galvanostatic charge–

discharge (GCD) curves of NCS-180//AC at different current densities, from which the specific capacitances were calculated to be 161.11, 132.62, 117.42, 106.00, 100.09, 95.56 F g^{-1} at current densities of 1, 2, 4, 6, 8 and 10 A g^{-1}, respectively. At a current density of 1 A g^{-1}, the energy density and power density of NCS-180//AC were determined to be 50.35 Wh kg^{-1} and 750 W kg^{-1}, respectively. When compared to recently reported asymmetric capacitors based on related nickel–cobalt sulfides, NCS-180//AC demonstrated higher or comparable energy densities, as illustrated in Fig. 8e and Table 2. The cycling stability of NCS-180//AC was evaluated at a current density of 10 A g^{-1} (Fig. 8f), revealing a capacity retention rate of 93.30% after 6000 cycles, which underscores the excellent cycling stability of NCS-180//AC.

Conclusions

In conclusion, this paper presents a one-step solvothermal method to synthesize nickel–cobalt sulfides using 1,4-dioxane as the solvent. The study explores the potential of this solvent with low coordination ability for creating bimetallic sulfides and identifies the optimal reaction temperature. The findings revealed that NiCo$_2$S$_4$ could be successfully synthesized at both 160 °C and 180 °C. The NiCo$_2$S$_4$ synthesized at 180 °C exhibited superior crystallinity and demonstrated enhanced cycling stability. The research results indicate that NCS-180 possesses a specific capacity of 664.30 C g^{-1} at a current density of 1 A g^{-1}, with a capacity retention rate of 77.42% at a current density of 10 A g^{-1}. Notably, it retains a capacity retention rate of 97.99% after 5000 cycles at a current density of 10 A g^{-1}. An asymmetric

Table 2 Comparison of energy density and power density between NCS-180//AC and other reported works

Devices	Energy density (Wh kg^{-1})	Power density (W kg^{-1})	Ref.
C-NCS/CC//AC	28	1105	42
NiCo$_2$S$_4$ NSs//N–C	26.9	375	47
CNCS-3//ACNFs	38.73	800	51
CoS$_2$/NiCo$_2$S$_4$/RGO//N–RGO	21.6	594.1	23
NiCo$_2$S$_4$/CNs-2//AC	49.7	818	52
NiCo$_2$S$_4$@MnO$_2$–V3//AC	39.7	775	25
Cu-NCS-10//KAC-5	46.3	775	53
NCS-180//AC	50.35	750	This work

supercapacitor was constructed employing NCS-180 as one electrode and activated carbon (AC) as the counter electrode. When operated at a power density of 750 W kg^{-1}, this device exhibited an energy density of 50.35 Wh kg^{-1}. Furthermore, following 6000 charge–discharge cycles at a current density of 10 A g^{-1}, the NCS-180//AC asymmetric supercapacitor retained a remarkable capacity retention rate of 93.30%. In comparison to NCSs described in prior literature, NCS-180 synthesized in this study exhibit different morphologies and good electrochemical performance. These findings underscore the viability of employing 1,4-dioxane as a solvent in the synthesis of NCSs, thereby contributing to the expansion of methodologies for the synthesis of such materials.

Author contributions

Yao Lei: writing – original draft, data curation, methodology. Qiwei Xu: software, supervision. Yiru Miao: funding acquisition, resources. Jiarong Shi: funding acquisition, methodology, writing – review & editing.

Conflicts of interest

There are no conflicts to declare.

Data availability

The authors confirm that the data supporting the findings of this study are available within the article and its SI. See DOI: https://doi.org/10.1039/d5ma00795j.

Notes and references

1 Y. Zhao, Q. Zhang, B. Sun, Y. Wang, X. Shu and Z. Dong, *J. Energy Storage*, 2024, **78**, 109995.

2 T.-Y. Wei, C.-H. Chen, H.-C. Chien, S.-Y. Lu and C.-C. Hu, *Adv. Mater.*, 2010, **22**, 347–351.

3 W. Zhang, X. Li, Z. Gu, H. Kang, Z. Li, B. Yang and Z. Li, *J. Alloys Compd.*, 2023, **969**, 172298.

4 J. Wang, Y. Xie, L. Wang, L. Wang, L. Yue and D. Jin, *Mater. Res. Bull.*, 2020, **131**, 110957.

5 T.-F. Yi, J.-J. Pan, T.-T. Wei, Y. Li and G. Cao, *Nano Today*, 2020, **33**, 100894.

6 F. Vaquero, R. M. Navarro and J. L. G. Fierro, *Appl. Catal., B*, 2017, **203**, 753–767.

7 G. Demazeau, *Z. Naturforsch.*, 2010, **65b**, 999–1006.

8 H. Chen, J. Jiang, L. Zhang, H. Wan, T. Qi and D. Xia, *Nanoscale*, 2013, **5**, 8879–8883.

9 Y. Zhang, M. Ma, J. Yang, C. Sun, H. Su, W. Huang and X. Dong, *Nanoscale*, 2014, **6**, 9824–9830.

10 J. Jiang, C. Yan, X. Zhao, H. Luo, Z. Xue and T. Mu, *Green Chem.*, 2017, **19**, 3023–3031.

11 C. Wei, Y. Huang, S. Xue, X. Zhang, X. Chen, J. Yan and W. Yao, *Chem. Eng. J.*, 2017, **317**, 873–881.

12 A. I. Abdel-Salam, S. Y. Attia, S. G. Mohamed, F. I. El-Hosiny, M. A. Sadek and M. M. Rashad, *Int. J. Hydrogen Energy*, 2023, **48**, 5463–5477.

13 Y. Zhang, Y. Chen, K. Liang, Y. Zhang, D. Wang, W. Wang, J. Wang, N. Mitsuzaki and Z. Chen, *J. Energy Storage*, 2025, **109**, 115176.

14 X. Wang, S.-X. Zhao, L. Dong, Q.-L. Lu, J. Zhu and C.-W. Nan, *Energy Storage Mater.*, 2017, **6**, 180–187.

15 W. Lu, M. Yang, X. Jiang, Y. Yu, X. Liu and Y. Xing, *Chem. Eng. J.*, 2020, **382**, 122943.

16 C. Wei, N. Zhan, J. Tao, S. Pang, L. Zhang, C. Cheng and D. Zhang, *Appl. Surf. Sci.*, 2018, **453**, 288–296.

17 B. Li, L. Zhang, Z. Zhao, Y. Zou, B. Chen, X. Fu, F. Wang, S. Long, W. Guo, J. Liang and M. Ye, *Chem. Eng. J.*, 2024, **487**, 150730.

18 H. Jia, M. Wang, M. Feng, G. Li, L. Li and Y. Liu, *Chem. Eng. J.*, 2024, **484**, 149591.

19 J. Xiao, H. Tong, F. Jin, D. Gong, X. Chen, Y. Wu, Y. Zhou, L. Shen and X. Zhang, *J. Power Sources*, 2022, **518**, 230763.

20 X. Wen, L. Xu, M. Chen, Y. Shi, C. Lv, Y. Cui, X. Wu, G. Cheng, C.-E. Wu, Z. Miao, F. Wang and X. Hu, *Appl. Catal., B*, 2021, **297**, 120486.

21 S. Hussain, N. Ullah, Y. Zhang, A. Shaheen, M. S. Javed, L. Lin, Zulfiqar, S. B. Shah, G. Liu and G. Qiao, *Int. J. Hydrogen Energy*, 2019, **44**, 24525–24533.

22 X. Xu, W. Zhong, L. Zhang, G. Liu and Y. Du, *J. Colloid Interface Sci.*, 2019, **556**, 24–32.

23 X. Li, W. Zhang, H. Kang, H. Liu, B. Yang, Z. Li and Z. Li, *J. Energy Storage*, 2023, **67**, 107528.

24 F. Xie, H. Zhu, Y. Qu, J. Hu, H. Tan, K. Wang and L. Sun, *J. Colloid Interface Sci.*, 2024, **657**, 63–74.

25 Q. Liu, C. Zhang, R. Li, J. Li, B. Zheng, S. Song, L. Chen, T. Li and Y. Ma, *J. Colloid Interface Sci.*, 2025, **678**, 902–914.

26 S. Zhang, J. Ren, T. Gu, H. Guo, H. Wang, M. Imran, R.-P. Ren and Y.-K. Lv, *Diamond Relat. Mater.*, 2022, **127**, 109154.

27 R. Dehghani-Abdoljabbar, H. Sharifpour, A. Kulkarni, S. Shahrokhian and D. P. Dubal, *ACS Appl. Energy Mater.*, 2025, **8**, 2779–2794.

28 Y. Luan, H. Zhang, F. Yang, J. Yan, K. Zhu, K. Ye, G. Wang, K. Cheng and D. Cao, *Appl. Surf. Sci.*, 2018, **447**, 165–172.

29 X. Huang, Y. Huang, G. Xu and X. Wang, *J. Power Sources*, 2023, **581**, 233488.

30 W. Cao, N. Chen, W. Zhao, Q. Xia, G. Du, C. Xiong, W. Li and L. Tang, *Electrochim. Acta*, 2022, **430**, 141049.

31 L. He, F. Wu, M. Bai, H. Ruan, L. Fang, J. Hu, H. Luo, S. Zhang, B. Hu and M. Zhou, *J. Alloys Compd.*, 2022, **908**, 164493.

32 H. Wang, X. Gao, Y. Xie, E. Guo, H. Bai, F. Jiang, Q. Li and H. Yue, *Adv. Energy Mater.*, 2024, **14**, 2400493.

33 M. Pathak, P. Mane, B. Chakraborty, J. S. Cho, S. M. Jeong and C. S. Rout, *Small*, 2024, **20**, 2310120.

34 M. F. Jimoh, G. S. Carson, M. B. Anderson, M. F. El-Kady and R. B. Kaner, *Adv. Funct. Mater.*, 2025, **35**, 2405569.

35 R. A. Mir, J. Xu, L. Tao, E. J. Hansen, A. Khosrozadeh, M. B. Miller and J. Liu, *Nano Energy*, 2025, **133**, 110446.

36 Y. Jiang and J. Liu, *Energy Environ. Mater.*, 2019, **2**, 30–37.

37 C. Lu, A. Li, T. Zhai, C. Niu, H. Duan, L. Guo and W. Zhou, *Energy Storage Mater.*, 2020, **26**, 472–482.

38 X. Yue, X. Li, Z. Ge, Y. Yang, Z. Zhao, T. Liu and H. He, *J. Electron. Mater.*, 2023, **52**, 7208–7220.

39 K. P. Shwetha, C. Manjunatha, M. K. Sudha Kamath, C. K. Rastogi, V. Chaudhary, G. Maurya, Y. Athreya, B. W. Shivaraj and A. Khosla, *J. Energy Storage*, 2023, **72**, 108657.

40 A. I. Abdel-Salam, S. Y. Attia, F. I. El-Hosiny, M. A. Sadek, S. G. Mohamed and M. M. Rashad, *Mater. Chem. Phys.*, 2022, **277**, 125554.

41 R. Bian, D. Song, W. Si, T. Zhang, Y. Zhang, P. Lu, F. Hou and J. Liang, *ChemElectroChem*, 2020, **7**, 3663–3669.

42 R. E. Mostafa, S. S. Mahmoud, N. S. Tantawy and S. G. Mohamed, *Chem. Eng. J.*, 2024, **481**, 148434.

43 H. Zhang, Y. Xie, S. Yang, X. Gao, H. Bai, F. Yao and H. Yue, *J. Alloys Compd.*, 2023, **968**, 171694.

44 S. S. Rabbani, H. Mustafa, A. Zafar, S. Javaid, M. A. Bakar, A. Nisar, Y. Liu, S. Karim, H. Sun, S. Hussain, Z. Zafar, Y. Faiz, F. Faiz, Y. Yu and M. Ahmad, *Electrochim. Acta*, 2023, **446**, 142098.

45 S. Ramesh, K. Karuppasamy, D. Vikraman, H. M. Yadav, H.-S. Kim, J.-H. Kim and H. S. Kim, *J. Energy Storage*, 2022, **55**, 105728.

46 R. S. Karmur, D. Gogoi, S. Sharma, M. R. Das, A. Dalvi and N. N. Ghosh, *J. Mater. Chem. A*, 2024, **12**, 12762–12776.

47 X. Zhang, Q. Zhao, T. Ma, Z. Li, X. Tan and B. Bateer, *J. Alloys Compd.*, 2023, **945**, 168902.

48 D. Wang, J. Wang, Y. Chu, S. Zha, Y. Chen, X. Du, N. Mitsuzaki, S. Jia and Z. Chen, *J. Energy Storage*, 2024, **96**, 112614.

49 S. Liu, Y. Zeng, M. Zhang, S. Xie, Y. Tong, F. Cheng and X. Lu, *J. Mater. Chem. A*, 2017, **5**, 21460–21466.

50 J. P. Cheng, S. Q. Gao, P. P. Zhang, B. Q. Wang, X. C. Wang and F. Liu, *J. Alloys Compd.*, 2020, **825**, 153984.

51 Z. Zhang, J. Wang, Z. Zhu, X. Ma, K. Fang, C. Wang, L. Kang, Z. Pan and G. Nie, *Sci. China Mater.*, 2023, **66**, 3484–3492.

52 P. Dong, X. Wu, Y. Lv, R. Xue, Y. Pei, N. Liang, H. Gao and J. Guo, *J. Colloid Interface Sci.*, 2025, **678**, 1036–1047.

53 K. Fan, X. Lei, J. Zhang, T. Tian, X. Song and H. Zhu, *J. Energy Storage*, 2024, **96**, 112572.